International Symposium
On Turbulence and Shear Flow
Phenomena (TSFP-8)
August 28 - 30, 2013 Poitiers, France

PIV INVESTIGATION OF SPANWISE VARIATION IN INCIDENT SHOCK BOUNDARY LAYER INTERACTIONS

Laura M. Campo
Dept. of Mechanical Engineering
Stanford University
488 Escondido Mall, Bldg 500
Stanford, CA 94305
lcampo@stanford.edu

David B. Helmer
Dept. of Mechanical Engineering
Stanford University
488 Escondido Mall, Bldg 500
Stanford, CA 94305
dhelmer@alumni.stanford.edu

John K. Eaton
Dept. of Mechanical Engineering
Stanford University
488 Escondido Mall, Bldg 500
Stanford, CA 94305
eatonj@stanford.edu

ABSTRACT

Two incident shock boundary layer interactions (SBLIs) were documented using high resolution 2D particle image velocimetry (PIV). The incident shock wave for each interaction was generated using a sub-boundary layer fully spanning 20° compression wedge on the top wall of the test section. A relatively weak SBLI occurred when the incident shock was generated using a 1.1mm ($0.20\delta_0$) high wedge, and a stronger interaction occurred when the incident shock was generated using a 3.0mm ($0.55\delta_0$) high wedge. For each SBLI, velocity and turbulence measurements were obtained in four planes across the span of a low aspect ratio test section – one near the center of the tunnel, and three inside the side wall boundary layer. The measurements indicated strong three-dimensionality in both interactions, with the interaction strength decreasing significantly near the side walls. Both interactions show regions of intermittent flow reversal, with the maximum value approximately tripled for the interaction generated by the larger wedge. Mean flow reversal was observed near the centerplane of the stronger SBLI, but not for the weaker SBLI.

INTRODUCTION

The complex flow phenomena involved in shock boundary layer interactions (SBLIs) are of interest at a fundamental level as well as for their application to practical systems including high speed flight vehicles. SBLIs are associated with shock wave unsteadiness, increased drag and heating, and shock induced boundary layer separation, all of which can have severe adverse effects on aerodynamic surfaces and propulsion systems. Shock induced boundary layer separation also is important in the unstart process in scramjet engines.

Many experimental studies of incident shock interactions have been conducted. Green (1970) used surface pressure measurements, Schlieren images, and oil flow measurements to study the reflection of incident shock waves of varying strengths ($2.5-10°$ degrees of flow deflection) from a turbulent boundary layer in a Mach 2.5 flow. This work indicated that a weak incident shock does not produce boundary layer separation and is reflected as a single shock wave with equal flow deflection to the incident shock. However, stronger incident shocks caused the boundary layer to separate and produced a complicated flow structure including a series of compression and expansion waves downstream of the reflected shock. Délery & Marvin (1986) summarize much of the early work on the reflected shock interaction.

More recent studies have applied a variety of techniques to document the incident shock interaction, many with emphasis on understanding the unsteadiness of the interaction. Dupont *et al.* examined Mach 2.3 interactions with deflection angles ranging from $7.5-9°$ using spark Schlieren, fast-response pressure transducers, and hot wire anemometry. They found that the nominally two-dimensional reflected shock oscillated in the streamwise direction over a distance comparable to the incoming boundary layer height, and that the frequency of this oscillation was much lower than the frequencies contained in the incoming boundary layer (Dupont *et al.* (2006)). Souverein *et al.* studied the relationship between incident shock wave strength and SBLI unsteadiness using both traditional PIV and dual-plane, time-resolved PIV. They concluded that unsteadiness in incipiently separated interactions was dependent on incoming boundary layer fluctuations while bubble dynamics controlled the unsteadiness of fully separated cases (Souverein *et al.* (2009) and Souverein *et al.* (2010)).

Humble *et al.* have characterized an incident SBLI produced by an 8° flow deflection in a Mach 2.1 flow (Humble *et al.* (2007). They also used tomographic PIV to study the instantaneous structure of an interaction produced by a 10° flow deflection in the same facility (Humble *et al.* (2009)). Their 3D measurements provide insight into the unsteady flow organization; however their measurement domain was confined to the center of the channel where the mean flow is nominally two-dimensional. The practice of focusing on

nominally two-dimensional interactions is common in previous experiments (see e.g. Settles & Dodson (1994) and Dolling (2001)). This is typically done by acquiring data far from the side wall boundary layers in the central region of large and/or high aspect ratio channels or by using aerodynamic fences to reduce side wall boundary layer effects. While much has been learned about the physics of SBLIs this way, the approach does not consider features of the SBLI structure that occur in regions near duct corners and within side wall boundary layers. A recent experiment by Helmer *et al.* (2012) confirmed that spanwise variations in the structure of a compression corner SBLI are significant and interesting, particularly for practical low-aspect ratio geometries. They noted distortion in the shock angle and structure as well as a significant reduction in interaction strength inside the side wall boundary layer. They also found non-monotonic trends in the mean and turbulent velocity statistics that were consistent with the presence of corner vortices. These data in the fully 3D interaction region are important for validation of codes and models used for 3D SBLI simulations.

The present experiment continues this study of spanwise variation by focusing on two incident SBLIs with incident shocks of different strengths. The specific objective was to examine and compare features of the mean and turbulent velocity statistics in the nominally two-dimensional centerplane and within the side wall boundary layer of a low aspect ratio duct. This was achieved by making high resolution planar PIV measurements in four streamwise-wall normal planes at varying spanwise locations.

EXPERIMENTAL SETUP

Facility

Experiments were performed in a continuously operated Mach 2.05 wind tunnel with a low aspect ratio test section (45mm×47.5mm). A side view schematic of the test section is shown in Figure 1. Continuous operation (vs. blowdown) allowed the flow to reach steady state before data collection and facilitated acquisition of large data records. The low aspect ratio and simple test section geometry were specifically chosen in order to make CFD simulations of the complete geometry feasible. The upstream stagnation temperature and pressure were controlled to maintain constant incoming flow conditions for the duration of each experiment.

The incident oblique shock wave was generated by a small compression wedge spanning the full width of the test section top wall. Wedges of two different heights, both inclined at an angle of 20°, were used to create SBLIs of varying strengths. The weaker of the two incident shocks was created by a 1.1mm tall wedge and the stronger shock was generated by a 3.0mm tall compression wedge. This geometry differs from the classic configuration of a sharp edged shock generating plate or wedge suspended in the freestream flow (see e.g. Délery & Marvin (1986)). In the current experiment, the small wedge sizes relative to the incoming boundary layer thickness ($0.20\delta_0$ and $0.55\delta_0$) were chosen in order to explore the influence of wedge height on the strength of the incident shock wave. The fact that the shock generating wedge is submerged in the boundary layer also means that viscous effects near the wedge are coupled to the overall structure of the shock wave, which affects the size and strength of the incident SBLI. The small wedge geometry also causes an expansion fan to be generated at the end of the compression wedge where the wall turns back to horizontal. Besides fundamental interest and relevance to practical applications, the combination of these features presents an interesting and challenging test case for CFD validation.

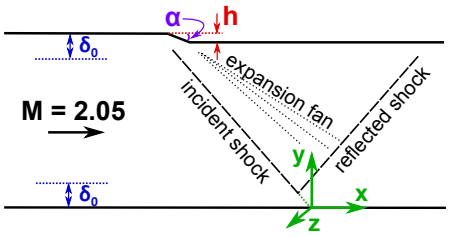

Figure 1. Side view of the test section showing prominent flow features and the coordinate system. The origin of the x-axis is the projected impingement location of the centerplane incident shock on the bottom wall.

Table 1. Inflow conditions & test setction geometry

$M_\infty = 2.05$	$U_\infty = 525$ m/s
$P_0 = 254 \pm 1.0$ kPa	$T_0 = 303 \pm 1$ K
$\delta_0 = 5.4$ mm	$\alpha = 20^\circ$
h (wedge heights):	1.1 mm & 3.0 mm
cross section (upstream):	45 mm × 47.5 mm

PIV Setup

Velocity measurements were made using two-component PIV in four streamwise-wall normal planes across the span of the test section. One measurement plane was near the tunnel centerline in the nominally 2D flow region ($z = 21$mm), one plane was at the edge of the side wall boundary layer ($z = 5.5$mm), and the other two measurement planes were located within the side wall boundary layer ($z = 4$mm, 2.5mm).

Aerosolized olive oil droplets were used to seed the flow. The particle response through a shock wave was examined in order to experimentally determine a particle time constant of $\tau_p \approx 1\mu$s. The particle Stokes number of $St = \tau_p U_\infty / \delta_{99} \approx 0.1$ indicates that these particles faithfully track the flow. The particles were introduced upstream of the flow conditioning section and converging-diverging nozzle to minimize flow disturbances. A 700μm thick laser sheet was produced by a NewWave Solo-200XT dual-pulse PIV laser with a wavelength of 532nm.

Images were acquired with a TSI model 630047 PIV camera with a 1024 × 1280 pixel array and a Nikon AF Micro-Nikkor 200 mm 1:4D lens. The frame delay between images was 800ns, and image pairs were acquired at a rate of 4Hz. For the smaller wedge case, the image resolution was 8.4μm/pixel, resulting in a field of view of 10.8mm × 8.6 mm per PIV tile. Data for the larger wedge case were taken at a lower image resolution of 15μm/pixel corresponding to a field of view of 19.2mm × 15.4mm per PIV tile. Due to the high resolution of the measurements, documentation of the full flow field was achieved by creating a composite of several overlapping tiles of PIV data in each plane. A minimum of 1500 images pairs were recorded for each PIV tile; in many tiles 5000 image pairs were captured. This large sample size allowed well-converged mean and turbulence statistics to be computed throughout the interaction region.

Table 2. PIV parameters

laser sheet thickness	0.7mm
inter-frame time	0.8μs
particle time constant	$\approx 1\mu$s
vector spacing	70 μm (1.1mm wedge)
	120 μm (3mm wedge)
vector overlap	50%
image pairs per tile	1500 – 5000
measurement planes	$z = 21$; 5.5; 4; 2.5 mm

Image data were processed using a conventional cross-correlation PIV algorithm with an iterative interrogation scheme with an initial size of 64×64 pixels and a final size of 16×16 pixels. The measurement resolution was 0.14×0.14mm^2 per velocity vector in the smaller 1.1mm wedge case and 0.24×0.24 mm^2 for the larger 3.0mm wedge. 50% overlap was used in both cases, resulting in vector spacings of approximately 0.07 mm and 0.12 mm respectively. Measurement parameters are listed in Table 2.

RESULTS

Inflow

The incoming freestream velocity near the channel centerline is $U_\infty = 525$ m/s ($M_\infty = 2.05$), and the undisturbed boundary layer upstream of the compression wedge has a thickness of $\delta_0 = 5.4$mm with a momentum thickness of $\theta = 450\mu$m. The corresponding Reynolds numbers are $Re_\delta \approx 80{,}000$ and $Re_\theta \approx 6700$. Detailed mean flow and turbulence data were acquired upstream of the interaction in order to verify that the inflow conditions were the same for both SBLI cases.

Mean velocity profiles of the incoming flow at a streamwise distance of 21mm upstream of the foot of the compression wedge are plotted in Figure 2. The velocity profile near the centerline ($z = 21$mm) shows a nearly asymptotic approach to the freestream velocity. The velocity profiles at $z = 5.5$, 4, and 2.5mm show a reduction in asymptotic velocity, which is expected since the profiles are embedded in the side wall boundary layer. In addition, these profiles show significant non-monotonic behavior with the magnitude of the overshoot increasing as the side wall is approached. The data are consistent with the presence of corner vortices as would be expected in a supersonic duct flow (see e.g. Davis & Gessner (1989)). Profiles of streamwise velocity fluctuations are shown in Figure 3. The turbulence profiles at all spanwise locations collapse within the region $0 < y/\delta_0 < 0.5$. Outside of this region the turbulence profiles at varying spanwise locations deviate from one another, with higher fluctuation levels closer to the side wall.

Incident Shock

The most prominent effect of the compression wedge height is that a larger wedge generates a stronger incident shock which increases the spatial extent and strength of the SBLI. Near the channel centerplane the angle of the incident shock wave generated by the larger (3.0mm high) wedge is 44.4°, as compared to 36.5° for the smaller (1.1mm high) wedge. Both shock angles are smaller than the 52° angle predicted by inviscid theory for a Mach 2.05 flow impinging on a 20° wedge. This is due to the small compression wedge

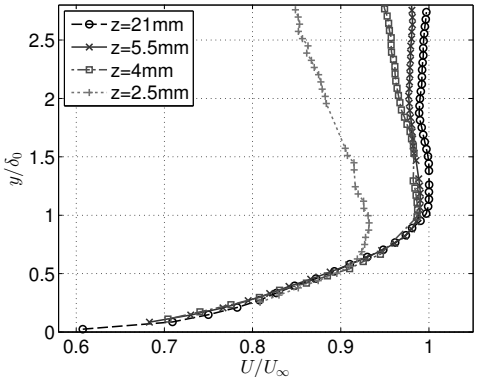

Figure 2. Incoming undisturbed boundary layer profiles (measured 21mm upstream of the compression wedge).

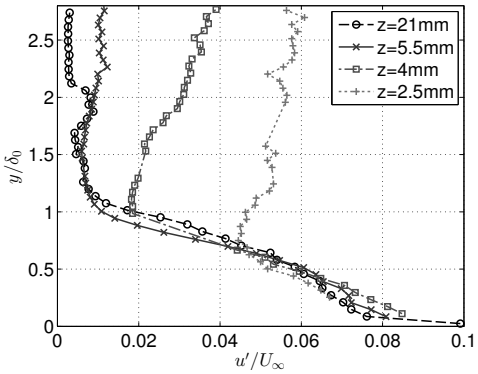

Figure 3. Incoming streamwise velocity fluctuation profiles (measured 21mm upstream of the compression wedge).

size and the fact that it is embedded in the top wall boundary layer.

The incident shock wave exhibits significant three-dimensionality across the span of the tunnel. For the smaller wedge case, the shock becomes very weak inside the side wall boundary layer and is difficult to identify. For the larger wedge case, the shock wave can clearly be identified in all four planes across the span. As the side wall is approached, the shock angle first steepens by a few degrees ($z = 5.5$ and 4mm planes) and then becomes more shallow ($z = 2.5$mm plane). Furthermore, in the side wall measurement planes the flow far from the bottom wall turns downward and then back toward horizontal before passing through the primary shock which causes the flow to turn downward again. This indicates the presence of an additional shock wave and expansion fan located slightly upstream of the primary oblique shock wave in the side wall planes.

Mean Velocity Contours

Figures 4 and 5 show the streamwise mean velocity component (U) and mean flow streamlines near the centerplane of the tunnel for both wedge geometries. The approximate mean sonic line (bold solid line) and the projected shock wave locations (dashed lines) have been plotted on top of the velocity contours and streamlines. The white area in Figure 4 is a region of low valid vector yield due to a stream of liquid on the imaging window which defocused particle images. Both interactions involve rapid boundary layer thickening followed by gradual boundary layer thinning downstream of the shock intersection point. The larger

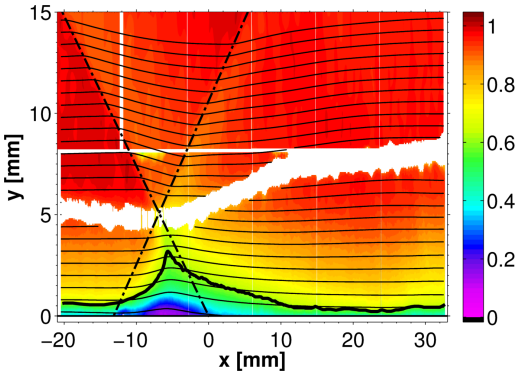

Figure 4. U/U_∞ near center plane for 1.1mm wedge.

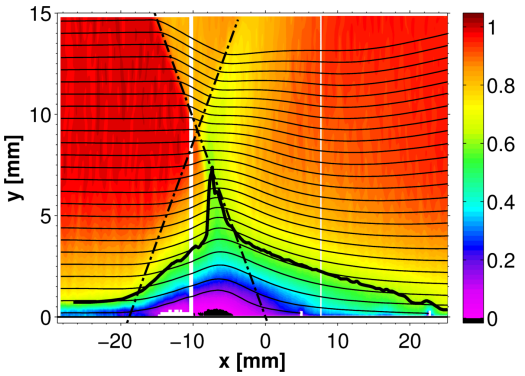

Figure 5. U/U_∞ near center plane for 3mm wedge.

wedge SBLI has a much greater spatial extent, and in particular the subsonic portion of the boundary layer extends about twice as far into the flow at its maximum height as compared to the smaller wedge SBLI.

Figures 6 and 7 show the mean streamwise velocity component inside the side wall boundary layer at z =4mm for both wedge geometries. The vertical white regions in these images correspond to areas where laser light was obstructed, and therefore the data have been masked. Other white areas indicate regions which had low yield of valid vectors due to reflections from the walls or low seeding density. The thickening and thinning of the boundary layer becomes far less prominent as the side wall of the tunnel is approached. In addition the overall interaction size decreases as the side wall is approached, and it is difficult to discern a precise location of the incident shock from the mean streamwise velocity plots. The dashed lines represent the locations of the incident and reflected shocks in the near centerplane data for reference.

The mean wall-normal velocity component (V) is shown for the 3mm wedge case near the centerplane (Figure 8) and in the $z = 4$mm plane (Figure 9). Note that the limits of the colorscale have been adjusted for the $z = 4$mm plane to better show the flow features. Near the centerplane, a single incident shock is evident, and there are two clear regions within the interaction corresponding to upward velocity (orange/red contours) and downward velocity (blue/purple contours). The strong vertical velocity component is consistent with the boundary layer thickening and thinning noted in Figure 5. In the $z = 4$mm plane, the magnitude of the vertical velocities are decreased throughout the region of interest, and the distinct regions of upward and downward velocity are no longer present.

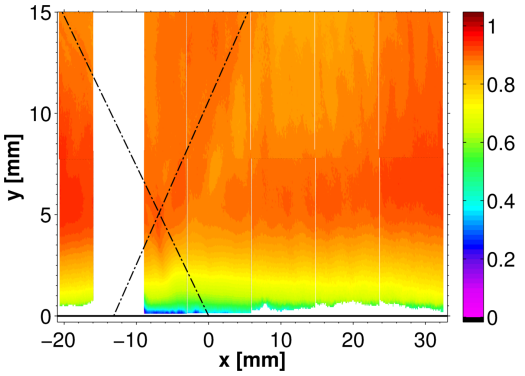

Figure 6. U/U_∞ at $z = 4$mm for 1.1mm wedge.

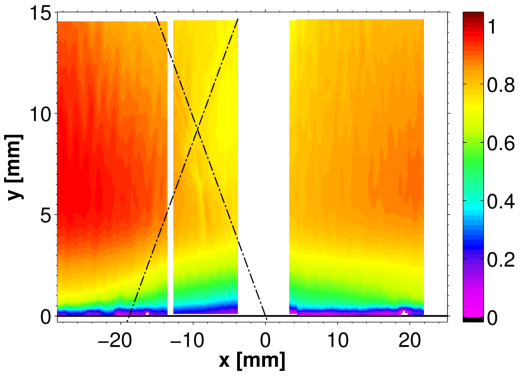

Figure 7. U/U_∞ at $z = 4$mm for 3.0mm wedge.

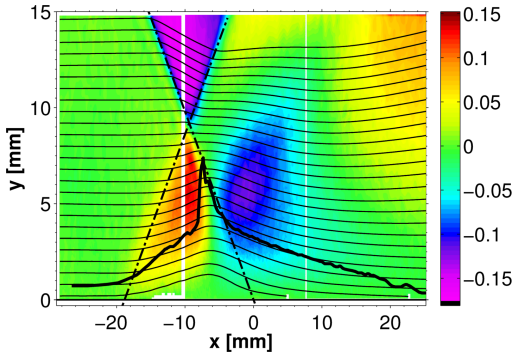

Figure 8. V/U_∞ near center plane for 3.0mm wedge.

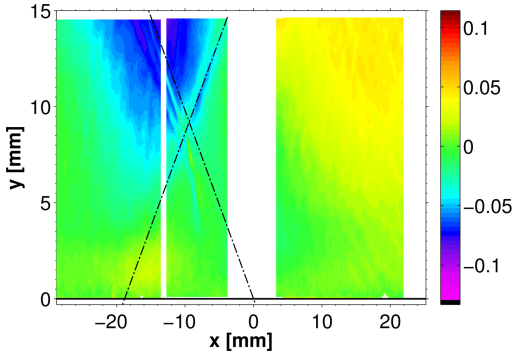

Figure 9. V/U_∞ at $z = 4$mm for 3.0mm wedge.

It is also interesting to note the structure of the incident shock wave, which is no longer a single distinct shock but rather a more gradual turning of the flow including a shock -

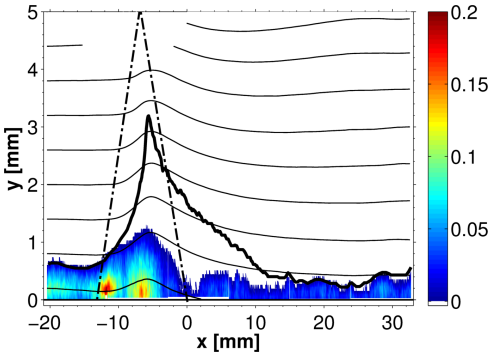

Figure 10. Probability of reversed flow near center plane for 1.1mm wedge.

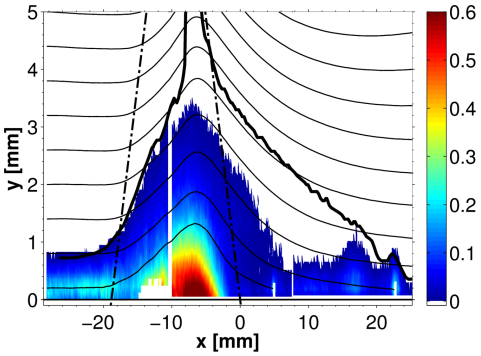

Figure 11. Probability of reversed flow near center plane for 3.0mm wedge.

expansion wave - shock structure. A similar structure is seen in the reflected wave pattern. These incident and reflected shock features occur upstream of their respective locations in the centerplane (indicated by the dashed lines). This suggests an overall curved structure of the incident shock in the spanwise direction near the side wall and is consistent with the steepening of the shock angle as the side wall is approached.

Flow Reversal

Figures 10 and 11 show the probability of instantaneous flow reversal near the centerline for both wedge geometries. Note that the wall-normal coordinate has been zoomed in to better show features close to the bottom wall. Streamlines (solid lines), projected shock locations (dashed lines), and the approximate sonic line (bolded line) have been overlaid. Both cases show regions of intermittent flow reversal, with the maximum value approximately tripled for the larger wedge case (60%) as compared to the smaller wedge (20%). The stronger shock generated by the larger wedge causes the region of instantaneous flow reversal to extend further from the bottom wall and a much greater deflection of the mean flow streamlines. The SBLI generated by the larger wedge also exhibits a small region of mean flow reversal near the centerplane (indicated by the black contours in Figure 5). No mean flow reversal is observed for this case in the side wall planes, and no mean flow reversal is observed anywhere in the SBLI generated by the 1.1mm wedge.

The magnitude and wall-normal extent of the reversing flow region decreases as the side wall is approached for both wedge cases. The obstruction of the flow near the centerline due to a region of intermittent or mean flow reversal causes high speed fluid to be diverted outward toward the side walls, which is consistent with the lesser degree of boundary layer thickening observed near the side walls.

Mean Velocity & Turbulence Profiles

In order to analyze the trends across the tunnel span more quantitatively, we examine profiles of mean velocity and turbulent fluctuations at two important streamwise locations. These locations are $x = -9.4$mm where the projected incident and reflected shocks intersect, and $x = -6.8$mm where maximum flow reversal occurs. Because many of the trends are similar and the flow features are more prominent for the larger wedge, only profiles for that case will be discussed.

Profiles of mean streamwise velocity at $x = -9.4$mm (projected shock intersection) are plotted in Figure 12. The

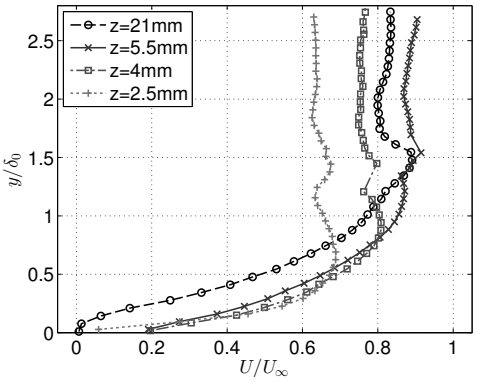

Figure 12. Profiles of mean streamwise velocity at $x = -9.4$mm (intersection of projected incident and reflected shocks for 3.0mm wedge).

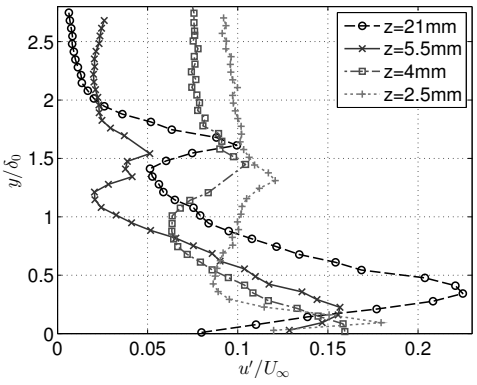

Figure 13. Profiles of streamwise velocity fluctuations at $x = -9.4$mm (intersection of projected incident and reflected shocks for 3.0mm wedge).

$z = 21$mm plane profile is inflectional, but does not include mean flow reversal. The velocity deficit in the profiles decreases monotonically as the side wall is approached, indicating that the thickening of the bottom wall boundary layer is less severe toward the side wall. Interestingly, the asymptotic velocity far from the bottom wall ($y/\delta_0 > 1.5$) does not follow a monotonic trend as the side wall is approached. This region of the flow is located above the shock intersection point downstream of the incident shock, and the streamwise velocity in the $z = 21$mm plane is lower than in the $z = 5.5$mm plane due to the much stronger shock that occurs

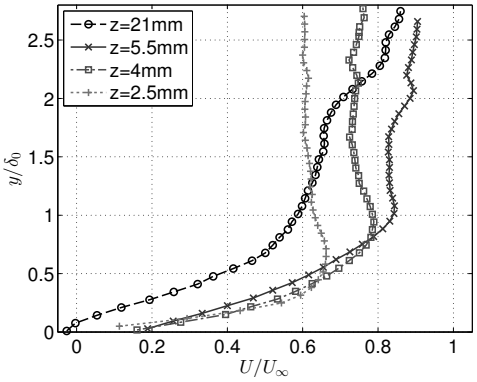

Figure 14. Profiles of mean streamwise velocity at $x = -6.8$mm (maximum flow reversal for 3.0mm wedge).

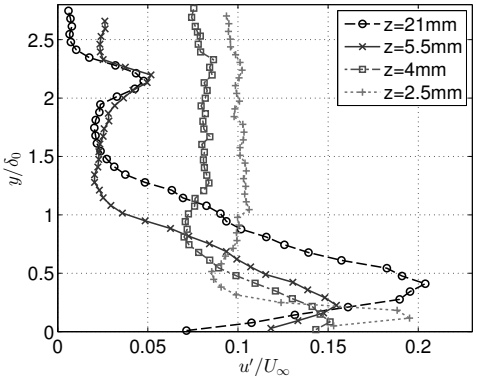

Figure 15. Profiles of streamwise velocity fluctuations at $x = -6.8$mm (maximum flow reversal for 3.0mm wedge).

at the center of the duct.

Profiles of streamwise velocity fluctuations at the same location ($x = -9.4$mm) are plotted in Figure 13. While the incoming turbulence profiles in each plane collapsed in the region $0 < y/\delta_0 < 0.5$, this is no longer the case inside the SBLI. The profile corresponding to each plane has a distinct peak which has been lifted away from the bottom wall. The width of this peak narrows and the maximum value occurs closer to the bottom wall as the side wall is approached; however there is no clear trend in the maximum value of turbulence. Each profile also has a local peak near $y/\delta_0 = 1.5$ which corresponds to the location where the shock wave is encountered in each plane. The $z = 5.5$mm profile has two local peaks which are consistent with a double shock wave structure near the side wall as was noted in Figure 9.

Profiles of streamwise mean velocity and fluctuations at $x = -6.8$mm (maximum flow reversal) are shown in Figures 14 and 15, respectively. The $z = 21$mm mean profile shows a small region of flow reversal near the bottom wall. The velocity defecit in this profile has grown significantly as compared to Figure 12; however the velocity defecits in the side wall profiles have remained nearly the same. Below $y/\delta_0 = 0.5$ the turbulence profiles look very similar to Figure 13. The peak in the $z = 21$mm and $z = 5.5$mm profiles near $y/\delta_0 = 2.2$ indicates that the reflected shock occurs at nearly the same location in these two planes. The absence of such a peak in the $z = 4$mm and $z = 2.5$mm profiles is due to the weaker reflected shock structure and the higher asymptotic values of streamwise turbulence away from the bottom wall.

Conclusion

PIV measurements of two incident SBLIs were taken in a Mach 2.05, continuously operated, low aspect ratio wind tunnel. The impinging shock for each case was generated by a sub-boundary layer compression wedge ($h = 1.1$mm and $h = 3.0$mm) inclined at 20°. The larger of the two wedges created a stronger incident shock which increased the overall size of the interaction and caused mean flow reversal near the center of the channel. The blockage of flow near the centerline diverted high speed fluid out toward the side walls. Combined with the weaker shock strength close to the side wall, this significantly mitigated the boundary layer thickening in the side wall measurement planes. A non-monotonic trend in the mean streamwise velocity profiles across the span was also attributed to the varying shock strength in the spanwise direction.

Acknowledgements

This work was supported by the Department of Energy (National Nuclear Security Administration) under Award Number NA28614. Additional support was received from the National Science Foundation Graduate Research Fellowship Program and the Gabilan Stanford Graduate Fellowship.

REFERENCES

Davis, D. & Gessner, F. 1989 Further experiments on supersonic turbulent flow development in a square duct. *AIAA Journal* **27**, 1023–1030.

Délery, J. & Marvin, J.G. 1986 Shock-wave boundary layer interactions. *AGARDograph* **280**.

Dolling, D.S. 2001 Fifty years of shock-wave/boundary-layer interaction research: What next? *AIAA Journal* **39**, 1517–1531.

Dupont, P., Haddad, C. & Debiève, J.F. 2006 Space and time organization in a shock-induced separated boundary layer. *J Fluid Mech* **559**, 255–277.

Green, J.E. 1970 Reflexion of an oblique shock wave by a turbulent boundary layer. *J Fluid Mech* **40**, 81–95.

Helmer, D.B., Campo, L.M. & Eaton, J.K. 2012 Three-dimensional features of a Mach 2.1 shock/boundary layer interaction. *Exp Fluids* **53**, 13471368.

Humble, R.A., Elsinga, G.E., Scarano, F. & van Oudheusden, B.W. 2009 Three-dimensional instantaneous structure of a shock wave/turbulent boundary layer interaction. *J Fluid Mech* **622**, 33–62.

Humble, R.A., Scarano, F. & van Oudheusden, B.W. 2007 Particle image velocimetry measurements of a shock wave/turbulent boundary layer interaction. *Exp Fluids* **43**, 173–183.

Settles, G.S. & Dodson, L.J. 1994 Supersonic and hypersonic shock/boundary-layer interaction database. *AIAA Journal* **32**, 1377–1383.

Souverein, L.J., Dupont, P., Debieve, J.F., Dussauge, J.P., van Oudheusden, B.W. & Scarano, F. 2010 Effect of interaction strength on unsteadiness in turbulent shock-wave-induced separations. *AIAA Journal* **48**, 1480–1493.

Souverein, L.J., van Oudheusden, B.W., Scarano, F. & Dupont, P. 2009 Application of a dual-plane particle image velocimetry (dual-piv) technique for the unsteadiness characterization of a shock wave turbulent boundary layer interaction. *Meas Sci Technol* **20**, 1–16.